Wind-Catalyzed Energy Exchanges between Fronts and Boundary Layer Turbulence

Zhihua Zheng,[a] Jacob O. Wenegrat,[a] Baylor Fox-Kemper,[b] Genevieve Jay Brett[c]

[a] *Department of Atmospheric and Oceanic Science, University of Maryland College Park, College Park, Maryland*

[b] *Department of Earth, Environmental, and Planetary Sciences, Brown University, Providence, Rhode Island*

[c] *Johns Hopkins University Applied Physics Laboratory, Laurel, Maryland*

Corresponding author: Zhihua Zheng, zhihua@umd.edu

ABSTRACT: The energy transfer from submesoscale fronts to turbulence through geostrophic shear production (GSP) is hypothesized to be a leading contributor to the forward energy cascade and upper ocean mixing. Current estimates of GSP are limited to scaling relations developed for forced symmetric instability (forced-SI), in which downfront winds are an important triggering mechanism. As not all winds are downfront, and not all fronts forced by downfront winds are in the forced-SI regime, the broader significance of GSP under forcing that differs from the forced-SI case remains uncertain. Here we investigate the magnitude and vertical structure of GSP across a range of wind-front configurations using Large Eddy Simulations. We find that the energy exchange between fronts and turbulence flows in either direction depending on the wind-front alignment. Moreover, the established scaling for the sum of GSP and vertical buoyancy flux remains valid regardless of the wind-front orientation. This generic behavior arises from a combination of turbulent Ekman balance and nearly vertically-uniform buoyancy evolution in the boundary layer. Under upfront winds, negative GSP results in an energy conversion from turbulence to fronts, and a reduction of dissipation relative to the no front case. An analytical model is used to quantify the upfront wind GSP and its effect on turbulence suppression. Under cross-front winds, with no additional buoyancy forcing, there is a compensation between GSP and potential energy conversion. These results have implications for boundary layer turbulence parameterizations at submesoscale fronts, and offer a more comprehensive understanding of GSP in the global kinetic energy budget.

1. Introduction

Ocean submesoscale motions are characterized by intense jets and vortices, sharp fronts, and filaments, roughly spanning horizontal scales of 0.1 to 10 km (McWilliams 2016; Gula et al. 2022; Taylor and Thompson 2023). Dynamically, these hydrographic features reside in a regime where planetary rotation, stratification and inertia are all important (Thomas et al. 2008), therefore serving as a key intermediary between large-scale balanced currents and small-scale unbalanced turbulence. The significance of submesoscales in connecting these two classes of motions is perhaps best reflected by its potential role in closing the global ocean energy budget. The classic three-dimensional (3D) turbulence theory predicts a forward energy cascade toward dissipation at very small scale (Kolmogorov 1941), whereas the quasi two-dimensional (2D) balanced currents are subject to an inverse energy cascade to even larger scales (Charney 1971; Salmon 1980). Consequently, mechanisms that can efficiently dissipate the energy of balanced geostrophic currents are crucial for sustaining a steady ocean circulation (Wunsch and Ferrari 2004; Ferrari and Wunsch 2009). Previous studies have shown that submesoscale processes can initiate a down-scale transfer of energy from large-scale circulation to small-scale turbulence and ultimately dissipative scales, thus completing the journey of forward cascade needed to balance the energy injected at large scales (Capet et al. 2008; Klein et al. 2008; Thomas and Taylor 2010; Molemaker et al. 2010; Skyllingstad and Samelson 2012; Chor et al. 2022; Srinivasan et al. 2022; Dong et al. 2024). The detail of energy transfer pathways at submesoscale range is complex and can violate typical parameterization assumptions such that models which do not resolve both the submesoscales and turbulence may not accurately represent the forward energy cascade (Taylor and Thompson 2023; Johnson and Fox-Kemper 2024).

Here we focus on the role of vertical geostrophic shear-induced energy exchanges between fronts and turbulence. This energy flux is commonly referred to as the geostrophic shear production (GSP), since it emerges as a shear production term in the turbulent kinetic energy (TKE) budget of boundary layers at fronts (see section 3). The importance of GSP for energy transfers has been frequently highlighted in the context of forced symmetric instability (forced-SI, e.g., Bachman et al. 2017). The instability drives a vertical momentum flux (or, Reynolds stress) down the gradient of geostrophic current, transferring energy from the geostrophic flow to eddy kinetic energy at a rate set by GSP. Forced-SI typically develops at strong fronts under destabilizing surface forcing when

3

the associated GSP is positive (i.e., a down-scale energy flux). Destabilizing forcing conditions can be triggered by a positive surface buoyancy flux ($B_0 > 0$) through surface cooling or evaporation, and more commonly, by wind stress τ_w directed downfront (i.e., aligned with the direction of the thermal wind shear). Downfront winds are destabilizing through a surface destruction of potential vorticity (PV, Thomas et al. 2008), which can be interpreted as resulting from a wind-driven cross-frontal Ekman buoyancy flux (EBF):

$$\text{EBF} = \frac{\tau_w \times \hat{\mathbf{k}}}{\rho_0 f} \cdot \nabla_h b, \tag{1}$$

where $\hat{\mathbf{k}}$ is the vertical unit vector (similarly, $\hat{\mathbf{i}}$ and $\hat{\mathbf{j}}$ will be used throughout to represent unit vectors in the cross-front and along-front direction), f is the Coriolis frequency, ρ_0 is a reference density, ∇_h denotes a horizontal gradient vector, and b is the buoyancy. Previous studies of forced-SI have shown that in these conditions the GSP is proportional to the EBF (Taylor and Ferrari 2010; Thomas and Taylor 2010; Thomas et al. 2013), providing a parameterization that has been applied in both observational and numerical studies (Thomas et al. 2016; Bachman et al. 2017; Buckingham et al. 2019; Dong et al. 2021).

Outside the downfront wind regime, the role of GSP has been less explored. Contrary to downfront winds, upfront winds blowing against the thermal wind shear have a stabilizing effect (EBF < 0) and promote restratification (Thomas and Ferrari 2008). One stabilizing wind case in the suite of forced simulations analyzed by Skyllingstad et al. (2017) indicates that SI can still develop beneath the Ekman-restratified layer, generating surface-decoupled turbulence via positive GSP in the lower part of the initial deep mixed layer with negative PV. However, the behavior of GSP in the upper stratified layer, as well as in scenarios with symmetrically stable fronts, was unaddressed. Yuan and Liang (2021) presented TKE budgets of simulations that span a wider range of wind-front orientations. Their results demonstrated that the sign, magnitude and vertical structure of GSP all vary with the wind-front angle, suggesting that GSP could be a universal cross-scale energy flux at submesoscale fronts. We argue below that this follows directly from the definition of the GSP–which requires only the joint existence of Reynolds stress and thermal wind shear–such that it is likely to be a ubiquitous aspect of frontal TKE budgets in the turbulent boundary layer.

GSP is important not only for its connection to the forward energy cascade from the balanced flow to the submesoscale, but also for its potential in modifying the boundary layer turbulence (D'Asaro et al. 2011; Thomas et al. 2013, 2016; Buckingham et al. 2019), which mediates the air-sea interaction and fluxes of momentum, heat and carbon between the ocean surface boundary layer (OSBL) and interior. For example, in conditions favorable for SI, most of the energy extracted from the front by GSP is subsequently lost to dissipation and diapycnal mixing via secondary Kelvin–Helmholtz shear instability (Taylor and Ferrari 2009; Chor et al. 2022). This represents a shift from the classic paradigm of atmosphere-driven turbulence, codified in traditional one-dimensional (1D) closure schemes used in general circulation models (GCMs) that depend on air-sea fluxes and surface waves (Li et al. 2019). These existing 1D boundary layer parameterizations (e.g., Large et al. 1994) fail to predict the intensity of the turbulence and mixing induced by large positive GSP (Dong et al. 2021) and tend to misrepresent the energy extraction from the resolved flow (Bachman et al. 2017). To address this, a new parameterization (Bachman et al. 2017) has to be invoked instead to account for the effects of SI in applications where the GCM has sufficient resolution to capture some, but not all, fronts and submesoscale instabilities. Recently, Dong et al. (2024) compared various TKE production terms using theory and outputs from a submesoscale-permitting global model, concluding that GSP is a globally significant source of energy for upper ocean mixing. However, work by Johnson and Fox-Kemper (2024) examining the influence of submesoscale flows on boundary layer turbulence shows that at fronts traditional 1D parameterizations are generally deficient in both downfront and upfront wind conditions. In stable regions forced by upfront winds, the average dissipation rate was about 20% less than that in regions with no front, suggesting a frontal sink of turbulence. These discrepancies may be linked to the GSP, whose effect is particularly less understood in conditions outside the forced-SI regime, hindering a comprehensive assessment of its effect on boundary layer turbulence at fronts and ultimately its role in the global energy budget.

To bridge these knowledge gaps, this study seeks to quantify and derive scaling for the GSP across a range of wind-front orientations using turbulence-resolving simulations. The manuscript is structured as follows: It begins with a description of the idealized numerical simulation setup in section 2. The role of GSP as a front-turbulence energy flux in the energetic framework is illustrated in section 3. A theoretical constraint for the GSP is described in section 4. Results

5

115 from the simulations are presented in section 5, organized into three groups: downfront winds,
116 cross-front winds, and upfront winds. For all three groups, diagnosed terms in the energy budget
117 are compared with the theoretical constraint introduced in section 4. Notably, we also propose a
118 new method to scale the GSP in upfront wind conditions. Section 6 summarizes the key points and
119 discusses the implications of the results.

2. Simulation setup

121 We use the Julia package Oceananigans (Ramadhan et al. 2020) to run a set of 3D LES with an
122 idealized frontal zone setup illustrated in Fig. 1. The computational domain has size $(L_x, L_y, L_z) =$
123 $(1000, 250, 100)$ m and uniform grid spacing $(\Delta x, \Delta y, \Delta z) = (1.25, 1.25, 0.3125)$ m in the cross-front
124 (x), along-front (y), and vertical (z) direction, respectively. The chosen grid resolution is sufficient
125 to resolve the Ozmidov scale and the results appear converged for all cases (see Appendix). Note
126 that the domain size in the along-front direction is too small to accommodate the development of
127 submesoscale mixed-layer instabilities (MLI, Boccaletti et al. 2007). This design simplifies the
128 multi-scale problem, enabling us to evaluate the turbulence energetics in a controlled environment
129 that is free from the additional complexities of MLI-induced vertical buoyancy flux (e.g., Yuan and
130 Liang 2021).

133 The front is represented by a fixed background state in which the along-front velocity $V_g(z)$ is in
134 thermal wind balance with the invariant buoyancy field $B(x)$,

$$f \frac{\partial V_g}{\partial z} = \frac{\partial B}{\partial x} = -M^2. \tag{2}$$

135 The horizontal buoyancy gradient M^2 describes the strength of the front and is kept constant in each
136 simulation. The nonhydrostatic incompressible Boussinesq equations for perturbations around the
137 background state are solved numerically using a finite volume discretization,

$$\frac{\partial \mathbf{u}}{\partial t} + (\mathbf{u} + V_g \hat{\mathbf{j}}) \cdot \nabla \mathbf{u} + w \frac{\partial V_g}{\partial z} \hat{\mathbf{j}} = -\nabla p + b \hat{\mathbf{k}} - \nabla \cdot \boldsymbol{\tau}, \tag{3}$$

$$\frac{\partial b}{\partial t} + (\mathbf{u} + V_g \hat{\mathbf{j}}) \cdot \nabla b - u M^2 = -\nabla \cdot \mathbf{F}, \tag{4}$$

138 where $\mathbf{u} = u_i = u\hat{\mathbf{i}} + v\hat{\mathbf{j}} + w\hat{\mathbf{k}}$ is the perturbation velocity [the subscript index $i = (1, 2, 3)$ marks
139 spatial coordinates], b is the perturbation buoyancy, p is the kinematic pressure, $\boldsymbol{\tau} = \tau_{ij}$ and
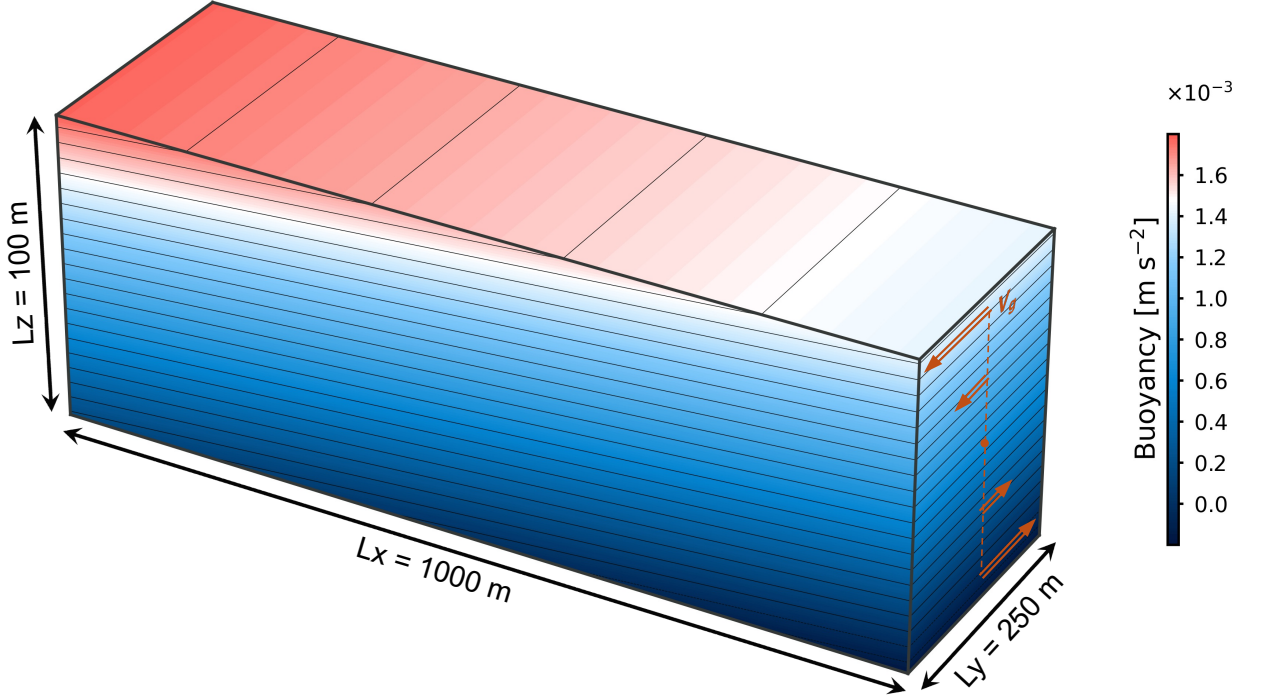
6

₁₃₁ FIG. 1. The simulation domain and the initial buoyancy field (for case DF1). Orange vectors on the side show
₁₃₂ the background geostrophic current.

₁₄₀ $\mathbf{F} = F_j$ with $i, j = (1, 2, 3)$ are the subgrid-scale (SGS) stress and buoyancy flux determined by a
₁₄₁ constant-coefficient Smagorinsky-Lilly closure[1] (Lilly 1962; Smagorinsky 1963). The perturbation
₁₄₂ buoyancy field is initialized with a uniform stratification $N^2 = \partial b/\partial z = 1.6 \times 10^{-5}$ s^{-2}, which, unlike
₁₄₃ M^2, evolves in time and space throughout the simulation. To speed up the transition to turbulence, a
₁₄₄ small-amplitude (1 mm s^{-1}) white noise is added to the initial perturbation velocity. The equations
₁₄₅ are then integrated forward with a second-order centered advection scheme and a third-order
₁₄₆ Runge–Kutta time-stepping method. We impose periodic boundary conditions for the perturbation
₁₄₇ variables in both horizontal directions and no normal flow in the vertical. At the bottom, no-stress
₁₄₈ boundary conditions are used for horizontal velocity components and the vertical buoyancy gradient
₁₄₉ is fixed to its initial value (N^2). The surface boundary conditions for the perturbation variables
₁₅₀ (u, v, b) are set by the wind stress[2] and surface buoyancy flux. To prevent spurious reflections of
₁₅₁ internal waves, a Gaussian-tapering sponge layer is placed at the bottom with a thickness of $L_z/5$.

---

[1]Note that the background thermal wind shear is not included in the closure calculation of eddy viscosity. This prevents the SGS scheme from causing excessive mixing during the initial non-turbulent phase (Taylor and Ferrari 2010).

[2]This formulation ignores the subgrid geostrophic stress at the surface, but its magnitude is negligible compared to the wind stress.

Since the perturbation fields are what the model solves for, we will omit the term 'perturbation' from variable names moving forward, noting that V_g and M^2 are tacitly ever present.

To investigate the variation of GSP in various wind-front configurations, the horizontal buoyancy gradient M^2, surface wind stress vector $\boldsymbol{\tau}_w = \tau_w^x \hat{\mathbf{i}} + \tau_w^y \hat{\mathbf{j}}$, and surface buoyancy flux B_0 are varied in the set of simulations described by Table 1. Overall, these include three groups of frontal zone simulations forced by downfront, upfront and cross-front winds, and two additional reference cases without a front. The wind stress is treated as an externally imposed forcing, and therefore it does not change in response to surface currents or temperature variations, both of which can alter the momentum and PV flux at fronts (Wenegrat 2023). All simulations start with a balanced Richardson number $\mathrm{Ri}_B = N^2 f^2 / M^4 > 1$. Given that the prescribed geostrophic flows also have no vertical relative vorticity, these fronts are initially stable to both SI and Kelvin–Helmholtz shear instability (Stone 1966). To minimize the inertial oscillation due to a sudden onset of wind forcing, the surface stress $\boldsymbol{\tau}_o$ is introduced with a smooth ramp-up before reaching the specified constant value $\boldsymbol{\tau}_w$,

$$\boldsymbol{\tau}_o(t) = 0.5\boldsymbol{\tau}_w \left[1 - \cos\left(\frac{\pi t}{\sqrt{2} T_f} \right) \right], \quad \text{for } 0 \le t \le \sqrt{2} T_f, \tag{5}$$

where $T_f = 2\pi/f$ is the inertial period. All simulations are run for three inertial periods and the diagnostics are saved every 5 minutes. We define a boundary layer using the depth at which the local stratification N^2 reaches maximum in the water column (Li and Fox-Kemper 2017). Alternatively, the turbulent boundary layer could be defined using turbulence statistics, such as the Reynolds stress magnitude (Wang et al. 2023) or the dissipation rate (Sutherland et al. 2014). However, we find the stratification-based method is more robust across different simulations, and is generally in line with the mixed layer depth computed from a density threshold method (Fig. 3), which is expected to match the turbulent boundary layer depth under steadily deepening surface conditions.

Group	Case	M^2 [s^{-2}]	τ_w^y [N m^{-2}]	τ_w^x [N m^{-2}]	EBF [m^2 s^{-3}]	B_0 [m^2 s^{-3}]	β	H/L_s	Comments
Downfront wind	DF1	3.6×10^{-7}	-0.037	0	-	1.3×10^{-7}	-	28	Forced-SI
	DF2	3×10^{-8}	-0.444	0	1.3×10^{-7}	0	-	0.89	No forced-SI
	DF3	9×10^{-8}	-0.148	0	1.3×10^{-7}	0	-	3.89	No forced-SI
Cross-front wind	CF1	9×10^{-8}	0	0.148	0	0	-	2.24	Warm to cold
	CF2	9×10^{-8}	0	-0.148	0	0	-	2.7	Cold to warm
Upfront wind	UF1	9×10^{-8}	0.148	0	-1.3×10^{-7}	0	8.01	1.73	-
	UF1c	9×10^{-8}	0.148	0	-1.3×10^{-7}	6.5×10^{-8}	7.61	2.52	-
	UF2	9×10^{-8}	0.444	0	-3.9×10^{-7}	0	9.80	1.73	-
	UF3	1.8×10^{-7}	0.148	0	-2.6×10^{-7}	0	7.74	2.7	-
	UF4	1.8×10^{-7}	0.444	0	-7.8×10^{-7}	0	9.76	2.81	-
	UF5	3.6×10^{-7}	0.444	0	-1.56×10^{-6}	0	9.37	4.09	-
No front	NF1	0	0	-0.148	0	0	7.96	0	-
	NF2	0	0	-0.444	0	0	9.55	0	-

3. Turbulent kinetic energy budget

179 For a boundary layer at the front, the turbulence kinetic energy (TKE) budget is expressed as

$$\underbrace{\frac{\partial k}{\partial t}}_{\text{Tendency}} = \underbrace{-\frac{\partial}{\partial z}\left(\langle w'u_i'u_i'\rangle/2 + \langle w'p'\rangle + \langle u_i'\tau_{i3}'\rangle\right)}_{\text{Turbulent, Pressure, and SGS Transport}} \underbrace{-\langle w'u'\rangle\frac{\partial\langle u\rangle}{\partial z} - \langle w'v'\rangle\frac{\partial\langle v\rangle}{\partial z}}_{\text{Ageostrophic Shear Production}} \underbrace{-\langle w'v'\rangle\frac{\partial V_g}{\partial z}}_{\text{GSP}}$$

$$\underbrace{+\langle w'b'\rangle}_{\text{Vertical Buoyancy Flux}} \quad \underbrace{-\varepsilon}_{\text{Dissipation}} \, , \tag{6}$$

180 where $k = \langle u_i'u_i'\rangle/2 = \langle u'^2 + v'^2 + w'^2\rangle/2$ is the TKE, $\langle \ \rangle$ represents a Reynolds average (whole-

181 domain horizontal average in our analysis), and prime denotes the turbulent fluctuation from that

182 average. Since our idealized simulations employ periodic boundary conditions and use whole-

183 domain horizontal averages as the Reynolds average, horizontal derivatives of mean turbulence

184 quantities do not appear in Eq. (6). This precludes the possibility of horizontal shear production

185 terms which may play an important role in the forward energy cascade through submesoscale

9

frontogenesis (Srinivasan et al. 2022; Yu et al. 2024), or other heterogeneous flow situations not considered here (e.g., Pearson et al. 2020; Brenner et al. 2023). Just like the ageostrophic shear production (ASP) representing the energy flux between mean ageostrophic flow and turbulence, GSP is the energy flux between geostrophic flow and turbulence. The same term with opposite sign also occurs in the equation for the mean cross-term kinetic energy, $\langle v \rangle V_g / 2$ (e.g., see Hilditch and Thomas 2023). For a frontal zone setup, GSP only evolves due to the along-front component of Reynolds stress $\langle w'v' \rangle$, as the geostrophic velocity V_g is fixed in time, thus GSP $= \langle w'v' \rangle M^2 / f$. We again emphasize that the only requirement for there to be a non-zero GSP is the joint presence of vertical momentum fluxes and thermal wind shear, both of which are universal features of submesoscale fronts in turbulent boundary layers. The vertical buoyancy flux (VBF) is the energy conversion rate between turbulent potential and kinetic energy.

In a quasi-steady state ($\partial k / \partial t \approx 0$), the relative magnitudes of various TKE budget terms at the mid-depth of the boundary layer can be roughly scaled by a set of dimensionless numbers (Li et al. 2005; Belcher et al. 2012; Li et al. 2019; Dong et al. 2024). In particular, following Monin and Obukhov (1954) in assuming the Reynolds stress is proportional to $u_*^2 = |\tau_w| / \rho_0$ (u_* is the waterside friction velocity), and the ageostrophic shear conforms to the law-of-the-wall scaling, the relative importance of GSP to ASP is measured by the ratio,

$$\frac{H}{L_s} = \frac{H M^2}{u_* f} = \frac{\Delta V_g}{u_*}, \tag{7}$$

where $L_s = u_* f / M^2$ is the geostrophic shear stability length (Skyllingstad et al. 2017), and according to the thermal wind relation, $\Delta V_g = H M^2 / f$ is the change in background geostrophic velocity across the boundary layer, whose depth H is here determined by the maximum vertical stratification. As such, this ratio also signifies the relative strength of the front and wind stress, $\Delta V_g / u_*$, which is a key parameter in determining the presence of forced-SI based on a theoretical scaling for the convective layer depth (Thomas et al. 2013). Here the scaling coefficient (e.g., used in Dong et al. 2024) is excluded for simplicity, so $H / L_s > 1$ does not necessarily mean larger GSP magnitude than ASP. But the value of H / L_s is still an effective comparative indicator of the relative GSP strength among simulations. For reference, the H / L_s for each simulation is shown in Table 1.

For each simulation, profiles of TKE budget terms are diagnosed and averaged in the last inertial period. Following Li and Fox-Kemper (2017), the time series of the horizontally-averaged diagnostics are interpolated to a common z/H grid before averaging in time so that "universal" profiles within the Monin and Obukhov (1954) similarity theory are reinforced rather than smeared out. Furthermore, this approach prevents the bias in the mean turbulence statistics that can arise from averaging data in the boundary layer with those not in the boundary layer during periods of deepening or shoaling.

4. Scaling of GSP + VBF

Under steady surface forcing, boundary layers at the front tend to reach a quasi-steady state, maintaining a consistent vertical buoyancy structure over time (i.e. the rate of change of buoyancy becomes independent of depth in the the boundary layer). Thus, the coupling between momentum and buoyancy through cross-front advection can be used to jointly constrain the combined effects of GSP and VBF (Taylor and Ferrari 2010). This scaling (restated below) originates from studies of forced-SI, however its relevance in non forced-SI conditions–particularly outside the downfront wind regime–has not been explored. Here, we demonstrate that this scaling is a generic feature of frontal boundary layers, at least to the extent the idealized simulation configuration used here is representative of more realistic frontal dynamics.

Consider the horizontally-averaged buoyancy budget and a turbulent Ekman balance in the cross-front momentum equation (see Taylor and Ferrari 2010), namely,

$$\frac{\partial \langle b \rangle}{\partial t} - M^2 \langle u \rangle = -\frac{\partial \langle w'b' \rangle}{\partial z} - \frac{\partial \langle F_3 \rangle}{\partial z}, \tag{8}$$

$$f \langle u \rangle = -\frac{\partial \langle w'v' \rangle}{\partial z} - \frac{\partial \langle \tau_{23} \rangle}{\partial z}. \tag{9}$$

Note that the stress in Eq. (9) is the total momentum flux down the gradients of both geostrophic and ageostrophic velocities, so the turbulent thermal wind (TTW) balance is implied (Wenegrat and McPhaden 2016). Integrating both Eq. (8) and (9) from z to 0 and eliminating terms involving $\langle u \rangle$ gives (following Thomas and Taylor 2010),

$$\langle w'v' \rangle \frac{M^2}{f} + \langle w'b' \rangle = \frac{-\tau_w^y}{\rho_0 f} M^2 + B_0 + \int_z^0 \frac{\partial \langle b \rangle}{\partial t} dz, \tag{10}$$

11

where the SGS terms have been neglected since they are only important near the surface. The first term on the right hand side is the EBF for a front configured as in Fig. 1, and the last term can be shown to scale with $\text{EBF} + B_0$ by setting the lower integral bound to $z = -H$. Assuming that the rate of change of $\langle b \rangle$ in the boundary layer is uniform with depth (consistent with the simulations shown below), and negligible[3] turbulent fluxes at $z = -H$, we have

$$\frac{\partial \langle b \rangle}{\partial t} = -\frac{\text{EBF} + B_0}{H}.$$ (11)

Finally, combining Eq. (10) and (11) yields

$$\text{GSP} + \text{VBF} = (\text{EBF} + B_0)(1 + z/H).$$ (12)

We also note that a similar result can be derived from the boundary layer PV budget (Taylor and Ferrari 2010), although interpreting PV in boundary layer LES requires caution (Bodner and Fox-Kemper 2020).

This scaling is expected to be valid as long as the vertical structure of the boundary layer (in terms of dimensionless depth z/H) is steady over time, and the ageostrophic mean flow reaches an Ekman balance. Indeed, the mean momentum and buoyancy budget in our simulations generally satisfy these two conditions. However, we emphasize that even if $\partial \langle b \rangle / \partial t$ is not strictly uniform in the boundary layer, then the relationship in Eq. (11) still constrains its vertical mean and thus the primary vertical structure of $\text{GSP} + \text{VBF}$ in the boundary layer. Any variations of $\partial \langle b \rangle / \partial t$ relative to its vertical mean, along with the finite values of fluxes at the boundary layer base, would lead to secondary variations of $\text{GSP} + \text{VBF}$ from the linear scaling.

At fronts there is thus a strong constraint that relates both the magnitude and basic vertical structure of the combined sum of GSP and VBF to the effective buoyancy forcing (air-sea plus Ekman buoyancy flux). Beyond this joint constraint, the GSP itself is also of particular independent interest as it represents a cross-scale energy flux between balanced larger-scale flows and turbulence. The method for isolating the GSP varies across different regimes, which we will highlight in the corresponding result section below.

---

[3]It is possible to include entrainment fluxes in the same theoretical framework, however we neglect these here as they are found to be small in the simulations considered (consistent with prior work on forced-SI such as Thomas et al. 2013). However, we do note that entrainment fluxes can be important in some specific cases (e.g., strong wind-driven deepening of the mixed layer during the passage of a storm, see Skyllingstad et al. 2000).
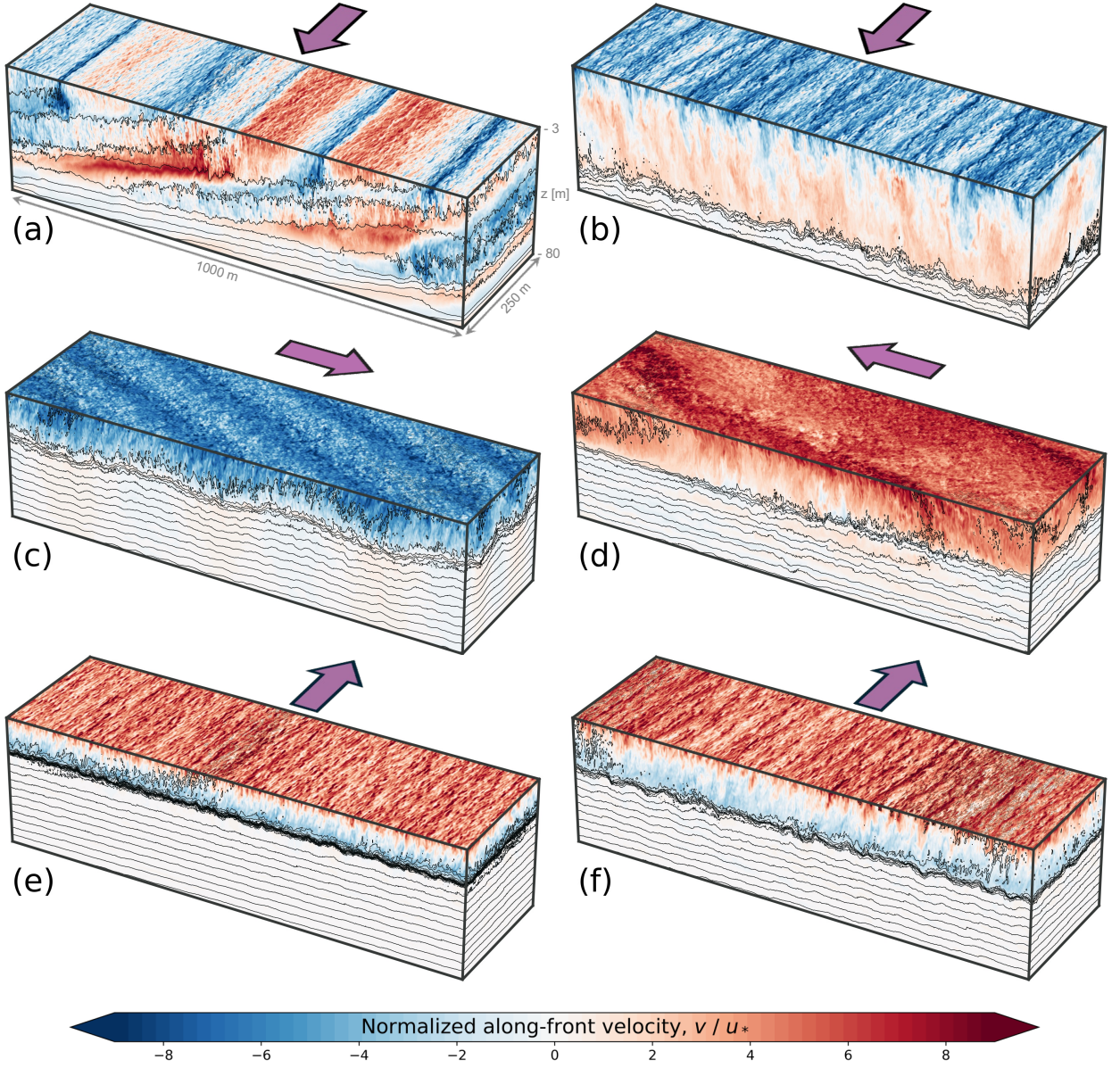
Fig. 2. Snapshots of the normalized along-front velocity v/u_* taken at about $2.86\,T_f$ for simulation case (a) DF1, (b) DF2, (c) CF1, (d) CF2, (e) UF1, (f) UF1c. The background geostrophic velocity is not included. Black lines show buoyancy contours with an interval of 8×10^{-5} m s^{-2}. Purple arrows show wind directions but their size do not represent wind stress magnitude. The upper 3 m are not plotted here for visual clarity. Animations of these simulations are available in the supplemental material.

5. Results

As the surface forcing varies across the simulations, the boundary layer at the front undergoes qualitatively different evolution (Figs. 2 and 3). Downfront winds [Figs. 2(a-b)] tend to generate

deeper boundary layers whereas upfront winds [Figs. 2(e-f)] induce restratification and confine the extent of turbulence to a shallower depth. Cross-front winds [Figs. 2(c-d)] can lead to mixed layers that are either shallower or deeper than the case with no front depending on the direction of the wind stress relative to the buoyancy gradient [Figs. 3(c-d)]. The different evolutions of the boundary layer depth can be interpreted through the PV budget, as a linear profile of GSP + VBF (Fig. 4) corresponds to a vertically uniform PV flux within the boundary (Taylor and Ferrari 2010). With no PV flux divergence in the boundary, surface PV extraction by downfront winds must be balanced by upward PV flux through the entrainment of high-PV water from the interior, leading to deepening of the low-PV layer. Conversely, surface PV injection by upfront winds must be transferred downward below the boundary layer, creating a high-PV layer near the boundary layer base. Snapshots of along-front velocity in Fig. 2 are representative of each wind-front alignment. Beyond the primary differences in $\langle v \rangle$ resulting from different wind directions, small-scale variations are also evident within each group, potentially linked to distinct modes of instability. The characteristics of each regime and the associated TKE budget are analyzed in detail in the following subsections.

a. Downfront winds

With downfront winds (EBF > 0), the boundary layer deepens with time [Figs. 3(a-b)], which might be a result of forced-SI [DF1 in Fig. 2(a)] or not [DF2 Fig. 2(b)]. The turbulence responsible for the deepening depends on the relative strength of the front and wind stress, measured by $\Delta V_g / u_*$. Consistent with previous studies, with $\Delta V_g > u_*$ in simulation DF1, GSP dominates the production of TKE and balances the dissipation [Fig. 4(a)], except in the upper 10% of the boundary layer. Fueled by this large down-scale energy flux from GSP, distinct "classic" SI patterns emerge as slanted cellular structures across the front [Fig. 2(a)], with the stratified SI layer occupying about 90% of the boundary layer [Fig. 3(a)]. In simulation DF2, since $\Delta V_g / u_*$ is much smaller, the wind-driven ASP is the most important source of TKE [Fig. 4(b)] so SI structures are not dominant, but GSP is still a source of turbulence and represents a non-negligible down-scale energy flux from geostrophic currents to turbulence. Haney et al. (2015) shows how energy budget contributions can be used to identify hidden instability mechanisms. According to the established understanding of this problem (Taylor and Ferrari 2010; Thomas et al. 2013), forced-SI is not expected to be dominant when $\Delta V_g / u_*$ is small. As anticipated, simulation DF2 has no classic phenomenological
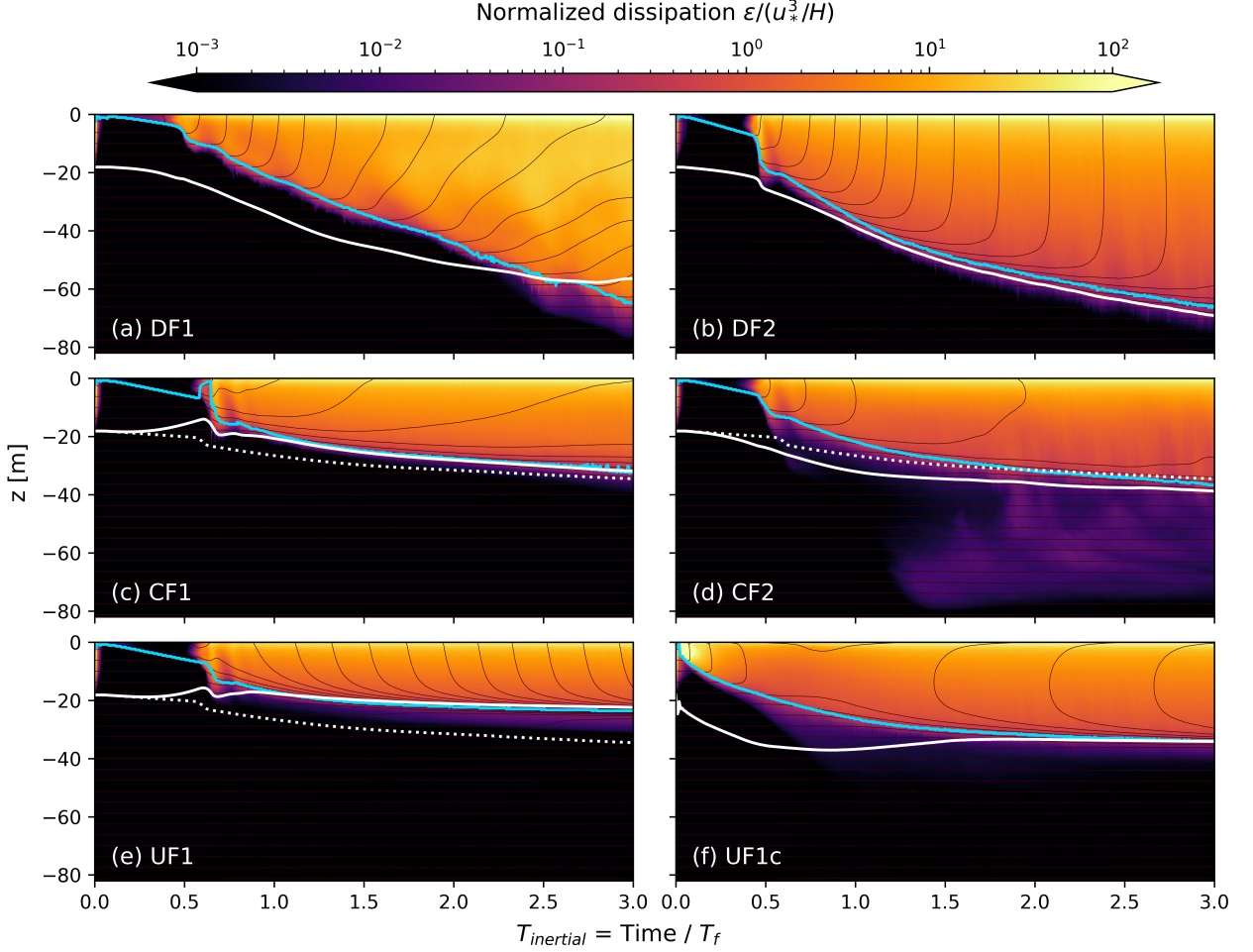
14

FIG. 3. Temporal evolution of the normalized TKE dissipation rate, $\varepsilon/(u_*^3/H)$, for simulation case (a) DF1, (b) DF2, (c) CF1, (d) CF2, (e) UF1, (f) UF1c. Note that the normalization by u_*^3/H is not intended to collapse the data but rather serves as a means to facilitate the comparison of results across different simulations. Black lines show buoyancy contours with an interval of 6×10^{-5} m s^{-2}. Cyan lines are the boundary layer depths H determined from maximum stratification. The mixed layer depths calculated using $\Delta b = 0.03$ g/ρ_0 m s^{-2} are shown in white for reference. Dotted white line is the mixed layer depth from the no front case NF1, which has the same wind stress magnitude as in case CF1, CF2, and UF1.

signs of SI (despite the non-negligible GSP), instead, the boundary layer is filled with smaller scale eddies and plumes, and remains unstratified throughout [Fig. 2(b)].

In both downfront wind simulations, the sum of GSP and VBF [Figs. 4(a-b)] generally agrees with the linear scaling [Eq. (12)]. The deviation from the linear scaling is slightly larger in case DF2, due to the strong entrainment flux near the bottom of boundary layer. Extra downfront wind

15

simulations with surface cooling (not shown) confirm that the linear scaling [Eq. (12)] is still valid, consistent with previous results (Thomas et al. 2013). Separating GSP from the combined scaling for GSP + VBF usually involves another scaling for the convective layer depth, which is used to estimate the VBF profile based on a linear decay of B_0 over the convective layer. For both simulations, since $B_0 = 0$, the magnitude of VBF is small, especially for the positive part [Figs. 4(a-b)], but the zero-crossing of the VBF profile occurs at a much shallower depth in DF1. This difference is consistent with the theoretical scaling of the convective layer depth (Taylor and Ferrari 2010). Therefore, for purely downfront wind cases, the GSP can be well approximated by EBF$(1 + z/H)$, and the vertically integrated GSP is roughly 0.5 EBF H—regardless of the presence of SI. Calculations using LES diagnostics [Fig. 6(b)] are in line with this bulk scaling, although the results from case DF2 and DF3 are slightly smaller, likely due to the entrainment flux neglected in the scaling. The success of the bulk scaling (regardless of the presence of SI or not) also provides support for the approach adopted by Dong et al. (2024) in estimating the contribution of downfront wind induced GSP to OSBL turbulence on a global scale.

b. Cross-front winds

The evolution of the boundary layer under cross-front winds depends on the wind direction (warm-to-cold, CF1, or, cold-to-warm, CF2), and in each case also differs significantly from the cases with winds aligned with the front. Although cross-front winds have zero EBF, they can still modify the near-surface stratification by generating a vertically sheared flow with nonzero cross-front component, initially due to frictional response, later through Ekman veering and turbulent thermal wind (TTW: Gula et al. 2014; Wenegrat and McPhaden 2016). The cross-front flow in this case, albeit small, can induce restratification and form a shallower mixed layer if directed toward the cold side [Fig. 3(c)]. On the contrary, if it is directed toward the warm side, destratification ensues, producing a slightly deeper mixed layer [Fig. 3(d)].

Interestingly, the ageostrophic flow in both simulations exhibits banded structures misaligned with the front and wind [Figs. 2(c-d)]. These structures are not evident in the no front simulation forced by the same wind. The characteristic wavelength of these features ranges from about 125 m in CF1 to about 250 m in CF2[4]. The signal is especially pronounced in CF2, where the

---

[4]Although CF2 only resolves about one wavelength of these banded structures, we have verified that their horizontal scale does not change significantly in larger domains.
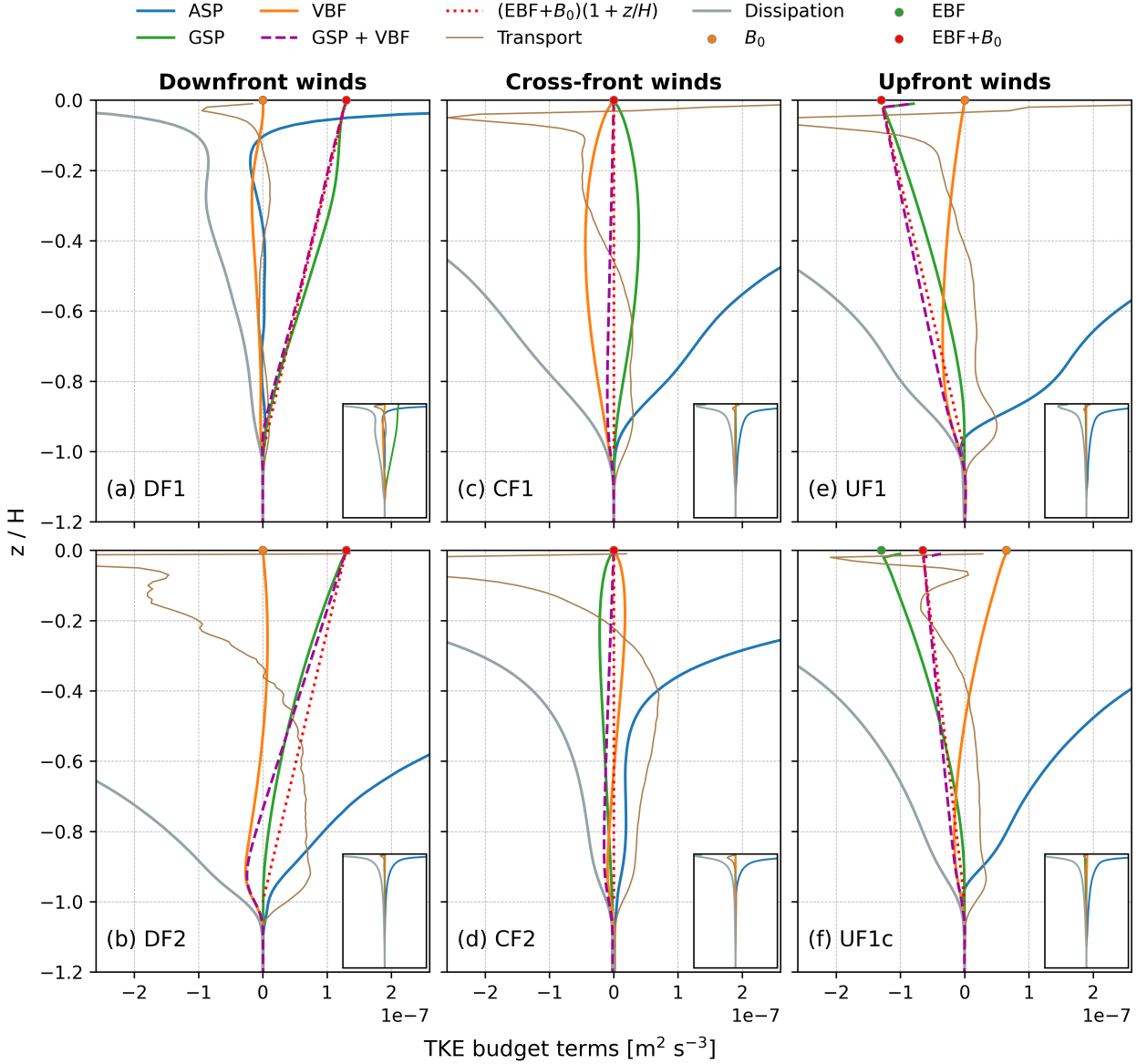
16

FIG. 4. TKE budget profiles averaged in the last inertial period for simulation case (a) DF1, (b) DF2, (c) CF1, (d) CF2, (e) UF1, (f) UF1c. All production terms include the SGS contribution. The transport term consists of turbulent, pressure, and SGS transport. The inset in each panel provides a zoomed-out view of the budget terms, bounded by the maximum magnitude, centered at zero.

coherent structures are linked to near-surface convergence at the edges of the rolls and localized energetic turbulence penetrating deep into the stratified layer. These tendril-like structures may also be responsible for the significantly higher dissipation rate below the boundary layer in CF2 [Fig. 3(d)]. It is possible that these structures are created by a mechanism that resembles the mixed

17

instability developed from the combined ageostrophic and geostrophic shear, as studied in detail by Skyllingstad et al. (2017) using a set of 2.5 by 2.5 km frontal zone LES. The dynamics of these coherent structures and their effects on vertical tracer transport are left for future work.

The sum of GSP and VBF in the cross-front wind regime [Figs. 4(c-d)] also match the linear scaling [Eq. (12)]. The seemingly trivial relationship here, GSP + VBF = 0, implies a compensation between them and a sign change of GSP as the cross-front winds switch direction. In the case of a warm-to-cold wind (CF1), the wind-driven ASP is the largest source for TKE, and the positive GSP provides the energy for the mixing of buoyancy. For a cold-to-warm wind (CF2), the negative GSP is balanced by the buoyancy production driven by the destabilizing advection of buoyancy. Thus, while there is no net effect of GSP + VBF on the TKE evolution, cross-front winds still generate an exchange between eddy potential energy and mean kinetic energy, which may affect frontal energetics and dynamics in ways not explored here.

We also note that in CF2, the ASP only dominates the TKE production in the upper half of the boundary layer, while the lower half has much weaker ageostrophic shear. The turbulence in the lower half is maintained by TKE transport from above. This feature is likely linked to the organized roll structures in Fig. 2(d). Previous studies of roll vortices in the atmospheric boundary layer have shown that this type of boundary layer scale motions are efficient in transporting momentum and energy (Etling and Brown 1993).

c. Upfront winds

With upfront winds (EBF < 0), the boundary layer always experiences a stabilizing buoyancy advection from the wind-driven shear flow. Meanwhile, the vertical stratification created by the cross-front shear flow is also being mixed away by the wind-driven turbulence. When these two effects reach a balance in the quasi-steady state, the vertical stratification within the boundary layer remains steady with time ($\partial N^2/\partial t \approx 0$). As a result, the wind-driven mixing is suppressed, and its vertical extent is limited to a shallow equilibrium depth [Figs. 3(e-f)]; the extra stratification induced by advection is transferred down below the boundary layer base, generating a pycnocline with growing strength over time (a feature which can also be interpreted in terms of PV dynamics, as above). Similar structure of the boundary layer was also reported in the upfront wind cases of Yuan and Liang (2021). In the following subsection, we show that under purely upfront winds, this

18

equilibrium depth scales with u_*/M. The restratification process is little changed with additional surface cooling, as long as $(\text{EBF} + B_0) < 0$. However, the surface cooling could aid the wind-driven turbulence to compete with the restratification, resulting in a deeper boundary layer [Fig. 3(f), and see Eq. (18)] and weaker stratification at the base of the boundary layer [Fig. 2(f)].

Similar to the other two groups, boundary layers in the upfront wind group exhibit a steady vertical stratification [Figs. 3(e-f)] and a turbulent Ekman balance (not shown). Consequently, the sum of GSP and VBF [Figs. 4(e-f)] closely follows the linear scaling [Eq. (12)], except near the surface, where the SGS effect is large. Note that this is a novel finding, as the theoretical constraint on GSP + VBF has not been previously examined in the upfront wind regime. From an energetic standpoint, ASP is the leading process in setting the turbulence energy level, whereas GSP acts as a sink of TKE. Here, negative GSP may not be interpreted as an indicator of up-gradient momentum flux from the geostrophic momentum. Instead, it reflects the work done on the geostrophic velocity by a wind-forced Reynolds stress that is decoupled from the geostrophic current. As the Reynolds stress rotates following the change of wind direction, while the thermal wind shear does not, GSP can take either sign, provided that the stress and thermal wind shear are independent of each other.

A negative GSP implies a sink of turbulence energy, and an upscale energy transfer, from small-scale turbulence to larger-scale currents. In our simulation setup, with imposed background buoyancy gradient, exact evidence of accelerated geostrophic current is hidden in the cross-term kinetic energy, $\langle v \rangle V_g / 2$, as the frontal zone setup does not allow changes in geostrophic velocity. For a freely evolving front, a reduction in the wind damping effect on the geostrophic current is expected. This is the upfront wind counterpart to the decrease of usable wind work for enhancing the kinetic energy of ocean circulation, caused by the positive GSP associated with downfront winds (Thomas and Taylor 2010).

Scaling upfront wind GSP

The method used to estimate downfront wind GSP may lack accuracy in the upfront wind regime for two reasons. First, the boundary layer can not be divided into two parts as for downfront winds; with surface cooling, even though there is a convective layer (with $\langle w'b' \rangle > 0$), the scaling for convective layer depth may become invalid. Second, in the case of $B_0 = 0$, the relative magnitude of VBF to GSP is still larger in upfront wind conditions than in downfront wind conditions,
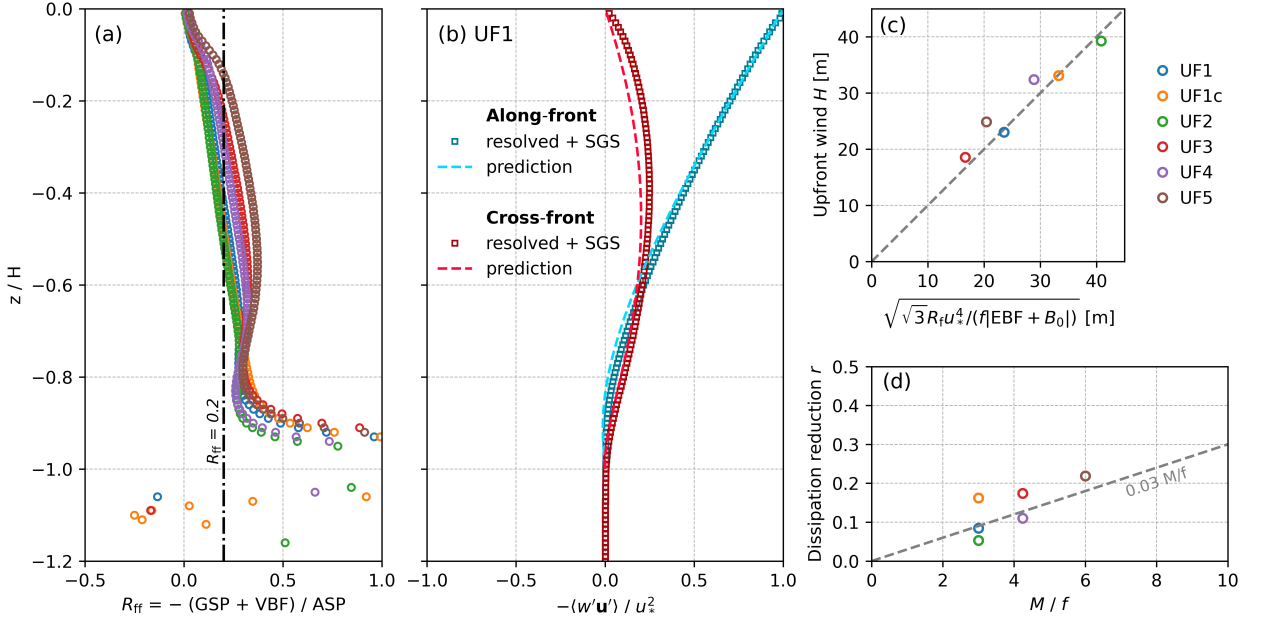
19

FIG. 5. (a) Profiles of frontal flux Richardson number R_{ff} for upfront wind cases. (b) Normalized Reynolds stress profiles in simulation case UF1 compared to the prediction by Eq. (17). (c) Scatter plot of boundary layer depths against predictions from the Derbyshire model [Eq. (18)]. (d) The percentage of reduction in dissipation as a function of simulation M/f. For each simulation, reduction of the vertically integrated dissipation is normalized by the reference value from the corresponding no front case [see Eq. (21)]. Data in all panels are averaged in the last inertial period.

therefore neglecting VBF would overestimate the magnitude of GSP. To that end, we propose a different method to estimate GSP in the upfront wind regime.

Here, we seek to quantify GSP directly through the along-front Reynolds stress $\langle w'v' \rangle$ (noting that M^2 is vertically uniform and hence does not contribute to the vertical structure of GSP). Since the effect of negative EBF in this case is similar to a stabilizing surface buoyancy flux and there is no submesoscale instability involved, we use a method adapted from the Derbyshire (1990) model for stable atmospheric boundary layers. The model assumes a quasi-steady boundary layer with turbulent Ekman balance in the momentum budget, and a constant ratio we term the frontal flux Richardson number, defined as

$$R_{ff} = \frac{-(\text{GSP} + \text{VBF})}{\text{ASP}}. \tag{13}$$

20

Unlike the traditional definition of flux Richardson number ($R_{\rm f} = -{\rm VBF/ASP}$), our approach includes GSP along with VBF, essentially comparing the relative contribution of these two production terms to the ASP. Although GSP is not a buoyancy flux in the strict sense, it can be considered as a hypothetical buoyancy flux due to its role in the mean buoyancy budget [Eq. (8)], such that the numerator of Eq. (13) can be thought of as the total effective buoyancy flux (Thomas and Lee 2005). The assumption of constant flux Richardson number is based on local equilibrium theory, which posits the existence of a critical value above which Kolmogorov turbulence can no longer be sustained (Zilitinkevich et al. 2010; Bou-Zeid et al. 2018). In our simulations $R_{\rm ff}$ is approximately constant for the bulk of the boundary layer [Fig. 5(a)], notwithstanding some variations that do not seem to greatly impact the applicability of the scaling. Hence, from the definition of the frontal flux Richardson number and the generic scaling [Eq. (12)] for GSP + VBF, we have

$$\mathcal{T}^* \frac{d\mathcal{M}}{dz} = \frac{({\rm EBF} + B_0)(1 + z/H)}{R_{\rm ff}}, \tag{14}$$

where * denotes complex conjugate, and the Reynolds stress $\mathcal{T} = \langle w'u'\rangle + i\langle w'v'\rangle$ and the vertical shear of the horizontal ageostrophic flow $\mathcal{M} = \langle u \rangle + i\langle v \rangle$ are assumed in parallel. The turbulent Ekman balance [see also Eq. (9)] can be written in complex notation as

$$\frac{d\mathcal{T}}{dz} = -if\mathcal{M}. \tag{15}$$

Taking the derivative of Eq. (15) and using Eq. (14) gives a second-order ordinary differential equation for the Reynolds stress,

$$\mathcal{T}^* \frac{d^2\mathcal{T}}{dz^2} = \frac{-if({\rm EBF} + B_0)(1 + z/H)}{R_{\rm ff}}. \tag{16}$$

With the boundary condition at the surface, $\mathcal{T}|_{z=0} = -iu_*^2$, and at the boundary layer base, $\mathcal{T}|_{z=-H} = 0$, the solution is given by

$$\mathcal{T} = -iu_*^2(1 + z/H)^{3/2 + i\sqrt{3}/2}. \tag{17}$$

21

434 Substituting the solution above back into Eq. (16) also yields an expression for the equilibrium
435 boundary layer depth,

$$H^2 = \frac{\sqrt{3} R_{\mathrm{ff}} u_*^4}{f |\mathrm{EBF} + B_0|}. \tag{18}$$

436 For purely upfront winds ($B_0 = 0$), this simplifies to the form

$$H = \sqrt{\sqrt{3} R_{\mathrm{ff}}} \frac{u_*}{M}. \tag{19}$$

437 For cases with surface heating but no front ($B_0 < 0$, EBF = 0), it reduces to a stratified Ekman
438 depth scaling $H = (\sqrt{3} R_{\mathrm{ff}} \kappa)^{1/2} (u_* L / f)^{1/2}$ (Zilitinkevich 1972), where $L = -u_*^3 / \kappa B_0$ is the Obukhov
439 length, with $\kappa = 0.4$ the von Kármán constant. Using a constant $R_{\mathrm{ff}} = 0.2$, Eq. (18) agrees well with
440 the boundary layer depth diagnosed from the maximum stratification [Fig. 5(c)]. For case UF3,
441 UF4 and UF5, the diagnosed H is a little larger than the prediction. These deviations are related
442 to the marginally larger R_{ff} in the boundary layer [Fig. 5(a)], and are potentially a result of slightly
443 under-resolving the Ozmidov scale near the base of the boundary layer [see Fig. A1(b)].

444 Figure 5(b) compares the Reynolds stress solution to that from simulation UF1. Overall, Eq. (17)
445 can effectively predict the Reynolds stress under upfront wind conditions, with particularly strong
446 accuracy for the along-front component, which is exactly the component needed to estimate GSP.
447 Introducing an upward surface buoyancy flux does not alter the shape of the Reynolds stress
448 profile significantly [see UF1c in Fig. 6(a)], and the largest change usually occurs in the crosswind
449 component. Therefore, we expect Eq. (17) remains valid even with nonzero surface buoyancy flux.
450 Unlike the prediction for the boundary layer depth, the stress prediction is independent of the value
451 of R_{ff} and should therefore remain robust, provided that R_{ff} has a weak depth dependence and H
452 is properly diagnosed.

457 Using the analytical solution for Reynolds stress $\mathcal{T}$ from Eq. (17), the vertically integrated GSP
458 in upfront wind conditions is

$$\int_{-H}^0 \mathrm{GSP}_{\mathrm{upfront\,wind}}\, dz = \int_{-H}^0 \mathrm{Im}(\mathcal{T}) \frac{M^2}{f}\, dz \approx 0.4\, \mathrm{EBF}\, H. \tag{20}$$

459 Since the Derbyshire model gives good prediction for the Reynolds stress, this bulk scaling for
460 GSP also agrees well with the numerical results from all upfront wind simulations [see Fig. 6(b)].
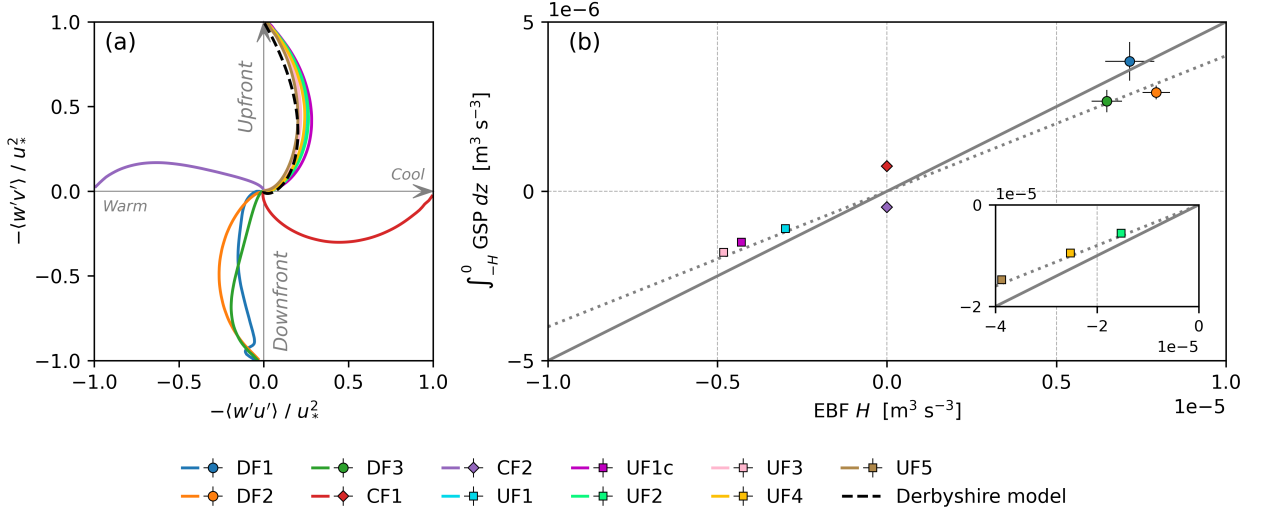
22

FIG. 6. (a) Hodographs of normalized Reynolds stress for all simulation cases. (b) Scatter plot of vertically integrated GSP against EBF H for all simulation cases. Gray lines correspond to 0.5 EBF H (solid) and 0.4 EBF H (dotted). The inset shows data outside the main axes limits. Error bars indicate standard deviations. Data in all panels include SGS stress terms, and are averaged in the last inertial period.

The scaling factor is very similar in magnitude to that in downfront forced-SI conditions (e.g. 0.5, Thomas et al. 2013), but here it represents a sink of TKE.

Given that the TKE source from ASP is about the same as the case with no front (Table 1), a negative GSP also suggests a reduction in dissipation rate. In fact, all upfront wind simulations analyzed here have smaller vertically integrated dissipation than the corresponding no front simulation forced by the same wind stress. The percentage of the reduction in the vertically integrated dissipation rate, defined as

$$r = 1 - \frac{\int_{-H}^{0} \epsilon_{\text{upfront wind}} \, dz}{\int_{-H}^{0} \epsilon_{\text{no front}} \, dz}, \tag{21}$$

is shown in Fig. 5(d) for each upfront wind simulation. For case Uf1c, the additional contribution to the integrated $\epsilon_{\text{no front}}$ from surface cooling is accounted for by an empirical scaling, $0.4 \, B_0 H$, proposed by Moeng and Sullivan (1994). This result is potentially relevant to the findings of Johnson and Fox-Kemper (2024), who argued that the turbulence suppression in the restratifying stable frontal region is stronger than the prediction by traditional (Monin and Obukhov 1954) 1D boundary layer scaling and parameterizations, due to the breakdown of the horizontal homogeneity

23

assumption. Since the vertical integral of ASP does not change significantly between the no front and the upfront wind simulation, the percentage of dissipation reduction can be estimated by the ratio

$$r \approx \frac{\int_{-H}^{0} \mathrm{GSP}_{\text{upfront wind}} \, dz}{\int_{-H}^{0} \mathrm{ASP} \, dz} = \frac{0.4}{\beta} \frac{\Delta V_g}{u_*}, \tag{22}$$

where the integrated dissipation is assumed to be in balance with the integrated ASP in the case of no front (Zippel et al. 2022), and $\beta = \int_{-H}^{0} \mathrm{ASP} \, dz / u_*^3 \approx 8$ is a coefficient calculated from the no front simulation NF1. Strictly speaking, β is not a constant, and appears to increase slightly with the magnitude of wind stress (e.g., $\beta \approx 9.6$ for NF2, see Table 1). However, for simplicity, we treat it as constant to derive an approximate estimate. For conditions represented by case UF1, Eq. (22) suggests a dissipation reduction of about 9%, which is consistent with the actual numerical simulation result in Fig. 5(d). If we assume the boundary layer depth scales with u_*/M under upfront winds [Eq. (19)], the dissipation reduction ratio becomes $r \approx 0.03 \, M/f$. In the upfront wind simulations, we do observe an increasing trend of dissipation reduction with M/f [Fig. 5(d)]. While this scaling for r is not perfect, it provides a conservative estimate of the dissipation reduction effect under various ocean conditions. For submesoscale fronts with M^2/f^2 typically ranging from order 10 to 100 (e.g., D'Asaro et al. 2011; Johnson et al. 2020), the reduction of dissipation due to negative GSP in the upfront wind regime is expected to be about 9–30%. This suppression effect could be even higher if the boundary layer is also forced by cooling or surface wave-driven turbulence counteracting the wind-driven restratification [as in case UF1c, see Fig. 5(d)].

6. Summary and Discussion

To better understand the exchange of energy between boundary layer turbulence and submesoscale fronts through the geostrophic shear production (GSP), we use a combination of theoretical arguments and Large Eddy Simulations (LES) to investigate the variability of GSP across a range of wind-front configurations, including downfront winds, cross-front winds and upfront winds. The key finding of this study is that GSP represents a generic energy flux between turbulence and fronts. The direction of the flux is determined by the wind-front alignment, while its magnitude is

24

governed by the effective buoyancy forcing and the boundary layer depth. In the remainder of this section, we will further elaborate on this concept and discuss its implications.

The best studied aspect of this energy exchange process is forced symmetric instability (forced-SI), which is viewed as an important mechanism for downscale energy transfer worthy of parameterization (Bachman et al. 2017). But because its onset depends critically on the strength of the fronts and the local surface forcing conditions such as downfront winds, its generality and overall contribution in the global forward energy cascade has been uncertain (e.g., Srinivasan et al. 2022). Here we show that GSP is not a special feature of forced-SI, instead, it is likely a generic cross-scale energy flux, due to the coexistence of Reynolds stress and vertical geostrophic shear in the turbulent boundary layer. This suggests that the route of forward energy cascade via GSP is not contingent on the presence of forced-SI. Thus, the GSP-associated forward energy cascade could initiate more quickly than SI–on the timescale of boundary layer turbulence–and occur under less stringent conditions that have been mostly overlooked, for example, when a strong downfront wind blows over a weak front. A corollary of this is that comparison of turbulent dissipation rate estimates with EBF-based scalings is not sufficient to conclude the presence of SI. High dissipation rates may correlate with the EBF even without active forced-SI. Future observational studies should incorporate additional diagnostic tools, such as the Thomas angle, convective depth ratio (Thomas et al. 2013; Taylor and Ferrari 2010) to better identify SI. While not the focus of this work, we also note that baroclinic flows along bottom topography can generate horizontal buoyancy gradients and turbulence, suggesting GSP may also provide a bi-directional cross-scale energy flux in the bottom boundary layer (Wenegrat et al. 2018; Wenegrat and Thomas 2020).

Depending on the orientation of the Reynolds stress and geostrophic shear, the energy exchange can flow in either direction–from front to turbulence or *vice versa*. Unlike downfront winds, upfront winds and cross-front winds aligned with the horizontal buoyancy gradient are typically associated with negative GSP and an upscale (turbulence-to-front) energy flux. Cross-front winds that oppose the horizontal buoyancy gradient tend to generate positive GSP. For a spatially complex field of fronts, or temporally varying surface winds, it is the combination of all local downscale and upscale flux that determines the net energy transfer. Considering only conditions favorable for forced-SI will misrepresent the total cross-scale energy flux.

Despite the disparate responses of the boundary layer in each case, we find that in all wind-front configurations, the sum of GSP and vertical buoyancy flux (VBF) scales with the combined Ekman and surface buoyancy fluxes, and decays linearly with depth according to Eq. (12). This behavior is consistent with the theoretical expectation of a quasi-steady boundary layer at the front. One limitation of the simulations considered here is that they do not resolve the mixed-layer instability (MLI), which has significant positive buoyancy flux to restratify the mixed layer. However, preliminary analysis of simulations in a large domain (still with fixed background buoyancy gradient) suggests that the theoretical constraint on GSP + VBF remains valid if the additional buoyancy forcing from MLI is accounted for. Extension of these findings to finite width fronts, which will allow for both the presence of horizontal shear production terms and for a response of the geostrophic flow to the GSP energy transfer, is left to future work (although note the fronts analyzed in Johnson and Fox-Kemper 2024, were finite width and exhibited many of the features highlighted here).

Together with the scaling for convective layer depth, the scaling for GSP + VBF could be used to estimate GSP under all downfront wind conditions. However, estimating GSP in other wind-front alignments necessitates a different approach. For upfront winds, we propose a method that can accurately predict Reynolds stress profile, thus GSP can be directly inferred. Compared to the purely downfront wind case, the upfront wind case has the same scaling, α EBF H, for the vertically integrated GSP, only that the coefficient $\alpha \approx 0.4$ is slightly smaller ($\alpha \approx 0.5$ for downfront winds). These effects are presently not captured in parameterizations where the presence of fronts is neglected by tradition in boundary layer schemes (Johnson and Fox-Kemper 2024). Comparison of this bulk scaling with GSP integrated from LES solutions [Fig. 6(b)] shows remarkable agreement for upfront winds, and reasonable agreement for downfront winds. The minor deviations in downfront wind cases are due to the neglect of VBF. Therefore, the major difference between the downfront and upfront wind induced GSP magnitude would likely come from the boundary layer depth H. With wind forcing alone, this difference in H can reach a factor of 2~3 within a few inertial periods. As a result, for a filament forced by the same along-front wind, the vertically integrated GSP at the two sides of the filament would be opposite in sign but asymmetric in magnitude, such that the spatial mean energy transfer would still be downscale (as found in Johnson and Fox-Kemper 2024).

26

For cross-front winds, EBF becomes less useful in scaling the vertically integrated GSP [Fig. 6(b)]. Although smaller in magnitude, the cross-front wind GSP may influence the net energy transfer by either offsetting or amplifying the GSP from along-front winds when the wind-front angle is oblique. It is worth noting that the cross-front wind opposing the horizontal buoyancy gradient produces a bit larger magnitude of GSP than the other one [Fig. 6(b)]. A potential explanation is that the wind-driven Ekman flows are in opposite directions, one strengthens the total along-front vertical shear while the other weakens it. As a result, the along-front Reynolds stress magnitude is larger in one case than the other, as is shown in Fig. 6(a). Furthermore, coherent roll structures are active in the cross-front wind regime examined here. In particular, those formed in the cold-to-warm wind scenario may play an important role in transporting energy and tracers into the ocean interior.

Since both components of the Reynolds stress scale with the wind stress, perhaps one can again use $\alpha u_*^2 \Delta V_g$ (note u_*^2 represents the full wind stress) to scale the vertically integrated GSP under cross-front wind conditions. Applying this method to our cross-front wind cases in this study suggests α is about 0.1 and 0.2 for the cold-to-warm and warm-to-cold wind case, respectively. Validating these empirical values will clearly require a broader exploration of the parameter space in the cross-front wind regime. The results here though suggest a limited range of $\alpha \approx 0.1 - 0.5$ for all wind orientations, such that the variation of α with wind-front alignment may be a secondary effect for the purpose of estimating bulk energy transfer rate, as compared to the strength of the wind and front. These variations in α are however obviously critical for tracer transport and mixing, as it reflects the change of the vertical structure of Reynolds stress profile with wind-front configuration [Fig. 6(a)]. Further investigation of this approach is beyond the scope of this paper and will be explored in future work.

Finally, we emphasize that these results are not only important for understanding the role of submesoscale fronts in the global kinetic energy budget, but also hold implications for boundary layer mixing parameterizations. In addition to the well studied forced-SI driven turbulence, we show that boundary layer turbulence is also modified by the presence of a front in conditions with no SI through the vertical shear production. This can be either a source or sink of TKE depending on wind direction, such that regional or global submesoscale-permitting models that rely on 1D turbulence parameterizations would alternately under or over estimate surface boundary

layer mixing, respectively. Existing parameterizations for submesoscale restratification via mixed-layer instability (Fox-Kemper et al. 2008), or geostrophic shear production restricted to forced-SI conditions (Bachman et al. 2017), will not properly represent this mechanism. This effect should be incorporated into boundary layer parameterizations; otherwise, excessive mixing of momentum in upfront wind conditions could feedback into the vertical shear, weakening fronts and misrepresenting forward energy transfer within the model.

Data availability statement. The simulation outputs for flow diagnostics, turbulence statistics, and the code used for setting up the simulation and analysis are available in the Zenodo repository (https://doi.org/10.5281/zenodo.15047812).

<div align="center">APPENDIX</div>

<div align="center">**Grid Resolution Sensitivity**</div>

To make sure our results do not vary significantly with grid resolution, we evaluate the vertical grid spacing Δz against the Ozmidov scale, defined as

$$L_{Ozmidov} = 2\pi\sqrt{\frac{\varepsilon}{N^3}}. \tag{A1}$$

The Ozmidov scale represents the largest length scale of 3D turbulence that conceptually remains free of stratification influences. Khani (2018) compared results from LES and and direct numerical simulation (DNS) and found that LES could correctly reproduce the directly resolved turbulent flow in DNS when the grid spacing is approximately equal or small to the Ozmidov scale. For boundary layers, especially the stratified ones, ε and N^2 vary significantly with depth, hence we compute vertical profiles of $L_{Ozmidov}$ using horizontally averaged ε and N^2 in turbulent regions ($\varepsilon > 10^{-10}$ m^2 s^{-3}) of the flow. Figures A1(a-b) show the profiles of $\Delta z/L_{Ozmidov}$ averaged in the last inertial period of all the simulations analyzed. Almost all of them satisfy or exceed the criteria ($\Delta z/L_{Ozmidov} \leq 1$) at all depth. Upfront wind cases are more challenging because the wind-driven restratification creates very strong N^2. Nevertheless, the chosen grid spacing is sufficient to resolve the Ozmidov scale through the bulk of the boundary layer.

To further test the convergence of results, we also run an extra set of the six main simulations with a 2 times coarser grid, but keeping the same grid aspect ratio $\Delta x : \Delta y : \Delta z$. Compared to the high resolutions runs used in the paper, these lower resolution runs have very similar integrated
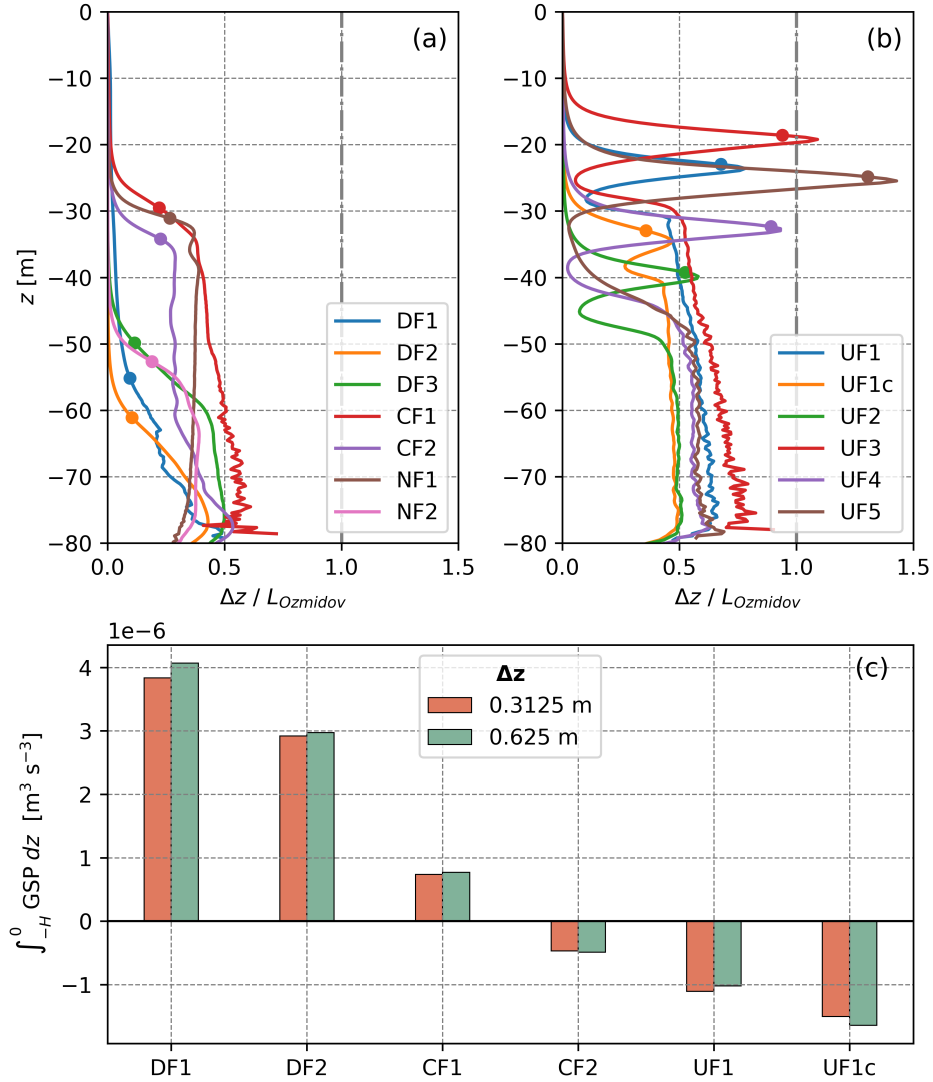
<div align="center">29</div>

FIG. A1. Mean profiles of $\Delta z / L_{Ozmidov}$ in the last inertial period for (a) non-upfront wind cases and (b) upfront wind cases. Dots denote the boundary layer depths. (c) Comparison of vertically integrated GSP from two sets of simulations with different Δz.

GSP values [Fig. A1(c)]. Therefore we consider our results converged and not sensitive to further refinement of grid resolution.

References

Bachman, S. D., B. Fox-Kemper, J. R. Taylor, and L. N. Thomas, 2017: Parameterization of Frontal Symmetric Instabilities. I: Theory for Resolved Fronts. *Ocean Modelling*, **109**, 72–95,

https://doi.org/10.1016/J.OCEMOD.2016.12.003.

Belcher, S. E., and Coauthors, 2012: A global perspective on Langmuir turbulence in the ocean surface boundary layer. *Geophysical Research Letters*, **39 (18)**, https://doi.org/10.1029/2012GL052932.

Boccaletti, G., R. Ferrari, and B. Fox-Kemper, 2007: Mixed Layer Instabilities and Restratification. *Journal of Physical Oceanography*, **37 (9)**, 2228–2250, https://doi.org/10.1175/JPO3101.1.

Bodner, A. S., and B. Fox-Kemper, 2020: A Breakdown in Potential Vorticity Estimation Delineates the Submesoscale-to-Turbulence Boundary in Large Eddy Simulations. *Journal of Advances in Modeling Earth Systems*, **12 (10)**, e2020MS002 049, https://doi.org/10.1029/2020MS002049.

Bou-Zeid, E., X. Gao, C. Ansorge, and G. G. Katul, 2018: On the role of return to isotropy in wall-bounded turbulent flows with buoyancy. *Journal of Fluid Mechanics*, **856**, 61–78, https://doi.org/10.1017/JFM.2018.693.

Brenner, S., C. Horvat, P. Hall, A. Lo Piccolo, B. Fox-Kemper, S. Labbé, and V. Dansereau, 2023: Scale-Dependent Air-Sea Exchange in the Polar Oceans: Floe-Floe and Floe-Flow Coupling in the Generation of Ice-Ocean Boundary Layer Turbulence. *Geophysical Research Letters*, **50 (23)**, e2023GL105 703, https://doi.org/10.1029/2023GL105703.

Buckingham, C. E., N. S. Lucas, S. E. Belcher, T. P. Rippeth, A. L. Grant, J. Le Sommer, A. O. Ajayi, and A. C. Naveira Garabato, 2019: The Contribution of Surface and Submesoscale Processes to Turbulence in the Open Ocean Surface Boundary Layer. *Journal of Advances in Modeling Earth Systems*, **11 (12)**, 4066–4094, https://doi.org/10.1029/2019MS001801.

Capet, X., J. C. McWilliams, M. J. Molemaker, and A. F. Shchepetkin, 2008: Mesoscale to Submesoscale Transition in the California Current System. Part III: Energy Balance and Flux. *Journal of Physical Oceanography*, **38 (10)**, 2256–2269, https://doi.org/10.1175/2008JPO3810.1.

Charney, J. G., 1971: Geostrophic Turbulence. *Journal of Atmospheric Sciences*, **28 (6)**, 1087 – 1095, https://doi.org/10.1175/1520-0469(1971)028⟨1087:GT⟩2.0.CO;2.

Chor, T., J. O. Wenegrat, and J. Taylor, 2022: Insights into the Mixing Efficiency of Submesoscale Centrifugal–Symmetric Instabilities. *Journal of Physical Oceanography*, **52 (10)**, 2273–2287, https://doi.org/10.1175/JPO-D-21-0259.1.

D'Asaro, E., C. Lee, L. Rainville, R. Harcourt, and L. Thomas, 2011: Enhanced turbulence and energy dissipation at ocean fronts. *Science*, **332 (6027)**, 318–322, https://doi.org/10.1126/SCIENCE.1201515.

Derbyshire, S. H., 1990: Nieuwstadt's stable boundary layer revisited. *Quarterly Journal of the Royal Meteorological Society*, **116 (491)**, 127–158, https://doi.org/10.1002/QJ.49711649106.

Dong, J., B. Fox-Kemper, J. O. Wenegrat, A. S. Bodner, X. Yu, S. Belcher, and C. Dong, 2024: Submesoscales are a significant turbulence source in global ocean surface boundary layer. *Nature Communications*, **15 (1)**, 1–11, https://doi.org/10.1038/s41467-024-53959-y.

Dong, J., B. Fox-Kemper, J. Zhu, and C. Dong, 2021: Application of Symmetric Instability Parameterization in the Coastal and Regional Ocean Community Model (CROCO). *Journal of Advances in Modeling Earth Systems*, **13 (3)**, e2020MS002 302, https://doi.org/10.1029/2020MS002302.

Etling, D., and R. A. Brown, 1993: Roll vortices in the planetary boundary layer: A review. *Boundary-Layer Meteorology*, **65 (3)**, 215–248, https://doi.org/10.1007/BF00705527.

Ferrari, R., and C. Wunsch, 2009: Ocean circulation kinetic energy: Reservoirs, sources, and sinks. *Annual Review of Fluid Mechanics*, **41 (Volume 41, 2009)**, 253–282, https://doi.org/10.1146/ANNUREV.FLUID.40.111406.102139.

Fox-Kemper, B., R. Ferrari, and R. Hallberg, 2008: Parameterization of Mixed Layer Eddies. Part I: Theory and Diagnosis. *Journal of Physical Oceanography*, **38 (6)**, 1145–1165, https://doi.org/10.1175/2007JPO3792.1.

Gula, J., J. J. Molemaker, and J. C. Mcwilliams, 2014: Submesoscale Cold Filaments in the Gulf Stream. *Journal of Physical Oceanography*, **44 (10)**, 2617–2643, https://doi.org/10.1175/JPO-D-14-0029.1.

Gula, J., J. Taylor, A. Shcherbina, and A. Mahadevan, 2022: Submesoscale processes and mixing. *Ocean Mixing: Drivers, Mechanisms and Impacts*, 181–214, https://doi.org/10.1016/B978-0-12-821512-8.00015-3.

Haney, S., B. Fox-Kemper, K. Julien, and A. Webb, 2015: Symmetric and Geostrophic Instabilities in the Wave-Forced Ocean Mixed Layer. *Journal of Physical Oceanography*, **45 (12)**, 3033–3056, https://doi.org/10.1175/JPO-D-15-0044.1.

Hilditch, J. P., and L. N. Thomas, 2023: Parametric subharmonic instability of inertial shear at ocean fronts. *Journal of Fluid Mechanics*, **966**, A34, https://doi.org/10.1017/JFM.2023.452.

Johnson, L., and B. Fox-Kemper, 2024: Modification of boundary layer turbulence by submesoscale flows. *Flow*, **4**, E20, https://doi.org/10.1017/FLO.2024.17.

Johnson, L., C. M. Lee, E. A. D'asaro, J. O. Wenegrat, and L. N. Thomas, 2020: Restratification at a California Current Upwelling Front. Part II: Dynamics. *Journal of Physical Oceanography*, **50 (5)**, 1473–1487, https://doi.org/10.1175/JPO-D-19-0204.1.

Khani, S., 2018: Mixing efficiency in large-eddy simulations of stratified turbulence. *Journal of Fluid Mechanics*, **849**, 373–394, https://doi.org/10.1017/JFM.2018.417.

Klein, P., B. L. Hua, G. Lapeyre, X. Capet, S. Le Gentil, and H. Sasaki, 2008: Upper Ocean Turbulence from High-Resolution 3D Simulations. *Journal of Physical Oceanography*, **38 (8)**, 1748–1763, https://doi.org/10.1175/2007JPO3773.1.

Kolmogorov, A. N., 1941: The Local Structure of Turbulence in Incompressible Viscous Fluid for Very Large Reynolds Numbers. *Dokl. Akad. Nauk SSSR*, **30**, 301–305.

Large, W. G., J. C. McWilliams, and S. C. Doney, 1994: Oceanic vertical mixing: A review and a model with a nonlocal boundary layer parameterization. *Reviews of Geophysics*, **32 (4)**, 363–403, https://doi.org/10.1029/94RG01872.

Li, M., C. Garrett, and E. Skyllingstad, 2005: A regime diagram for classifying turbulent large eddies in the upper ocean. *Deep Sea Research Part I: Oceanographic Research Papers*, **52 (2)**, 259–278, https://doi.org/10.1016/J.DSR.2004.09.004.

Li, Q., and B. Fox-Kemper, 2017: Assessing the effects of Langmuir turbulence on the entrainment buoyancy flux in the ocean surface boundary layer. *Journal of Physical Oceanography*, **47 (12)**, 2863–2886, https://doi.org/10.1175/JPO-D-17-0085.1.

Li, Q., and Coauthors, 2019: Comparing Ocean Surface Boundary Vertical Mixing Schemes Including Langmuir Turbulence. *Journal of Advances in Modeling Earth Systems*, **11 (11)**, 3545–3592, https://doi.org/10.1029/2019MS001810.

Lilly, D. K., 1962: On the numerical simulation of buoyant convection. *Tellus*, **14 (2)**, 148–172, https://doi.org/10.1111/J.2153-3490.1962.TB00128.X.

McWilliams, J. C., 2016: Submesoscale currents in the ocean. *Proceedings of the Royal Society A: Mathematical, Physical and Engineering Sciences*, **472 (2189)**, https://doi.org/10.1098/RSPA.2016.0117.

Moeng, C.-H., and P. P. Sullivan, 1994: A Comparison of Shear- and Buoyancy-Driven Planetary Boundary Layer Flows. *Journal of Atmospheric Sciences*, **51 (7)**, 999 – 1022, https://doi.org/10.1175/1520-0469(1994)051⟨0999:ACOSAB⟩2.0.CO;2.

Molemaker, M. J., J. C. McWilliams, and X. Capet, 2010: Balanced and unbalanced routes to dissipation in an equilibrated Eady flow. *Journal of Fluid Mechanics*, **654**, 35–63, https://doi.org/10.1017/S0022112009993272.

Monin, A. S., and A. M. Obukhov, 1954: Basic laws of turbulent mixing in the surface layer of the atmosphere. *Contrib. Geophys. Inst. Acad. Sci. USSR*, **24 (151)**, 163–187.

Pearson, J., and Coauthors, 2020: Biases in Structure Functions from Observations of Submesoscale Flows. *Journal of Geophysical Research: Oceans*, **125 (6)**, e2019JC015 769, https://doi.org/10.1029/2019JC015769.

Ramadhan, A., and Coauthors, 2020: Oceananigans.jl: Fast and friendly geophysical fluid dynamics on GPUs. *Journal of Open Source Software*, **5 (53)**, 2018, https://doi.org/10.21105/JOSS.02018.

Salmon, R., 1980: Baroclinic instability and geostrophic turbulence. *Geophysical & Astrophysical Fluid Dynamics*, **15 (1)**, 167–211, https://doi.org/10.1080/03091928008241178.

Skyllingstad, E. D., J. Duncombe, and R. M. Samelson, 2017: Baroclinic Frontal Instabilities and Turbulent Mixing in the Surface Boundary Layer. Part II: Forced Simulations. *Journal of Physical Oceanography*, **47 (10)**, 2429–2454, https://doi.org/10.1175/JPO-D-16-0179.1.

Skyllingstad, E. D., and R. M. Samelson, 2012: Baroclinic Frontal Instabilities and Turbulent Mixing in the Surface Boundary Layer. Part I: Unforced Simulations. *Journal of Physical Oceanography*, **42 (10)**, 1701–1716, https://doi.org/10.1175/JPO-D-10-05016.1.

Skyllingstad, E. D., W. D. Smyth, and G. B. Crawford, 2000: Resonant Wind-Driven Mixing in the Ocean Boundary Layer. *Journal of Physical Oceanography*, **30 (8)**, 1866 – 1890, https://doi.org/10.1175/1520-0485(2000)030⟨1866:RWDMIT⟩2.0.CO;2.

Smagorinsky, J., 1963: General circulation experiments with the primitive equations: I. The basic experiment. *Monthly Weather Review*, **91 (3)**, 99 – 164, https://doi.org/10.1175/1520-0493(1963)091⟨0099:GCEWTP⟩2.3.CO;2.

Srinivasan, K., R. Barkan, and J. C. McWilliams, 2022: A Forward Energy Flux at Submesoscales Driven by Frontogenesis. *Journal of Physical Oceanography*, **53 (1)**, 287–305, https://doi.org/10.1175/JPO-D-22-0001.1.

Stone, P. H., 1966: On Non-Geostrophic Baroclinic Stability. *Journal of Atmospheric Sciences*, **23 (4)**, 390 – 400, https://doi.org/10.1175/1520-0469(1966)023⟨0390:ONGBS⟩2.0.CO;2.

Sutherland, G., G. Reverdin, L. Marié, and B. Ward, 2014: Mixed and mixing layer depths in the ocean surface boundary layer under conditions of diurnal stratification. *Geophysical Research Letters*, **41 (23)**, 8469–8476, https://doi.org/10.1002/2014GL061939.

Taylor, J. R., and R. Ferrari, 2009: On the equilibration of a symmetrically unstable front via a secondary shear instability. *Journal of Fluid Mechanics*, **622**, 103–113, https://doi.org/10.1017/S0022112008005272.

Taylor, J. R., and R. Ferrari, 2010: Buoyancy and Wind-Driven Convection at Mixed Layer Density Fronts. *Journal of Physical Oceanography*, **40 (6)**, 1222–1242, https://doi.org/10.1175/2010JPO4365.1.

Taylor, J. R., and A. F. Thompson, 2023: Submesoscale Dynamics in the Upper Ocean. *Annual Review of Fluid Mechanics*, **55 (Volume 55, 2023)**, 103–127, https://doi.org/10.1146/ANNUREV-FLUID-031422-095147.

Thomas, L., and R. Ferrari, 2008: Friction, Frontogenesis, and the Stratification of the Surface Mixed Layer. *Journal of Physical Oceanography*, **38 (11)**, 2501–2518, https://doi.org/10.1175/2008JPO3797.1.

Thomas, L. N., and C. M. Lee, 2005: Intensification of Ocean Fronts by Down-Front Winds. *Journal of Physical Oceanography*, **35 (6)**, 1086–1102, https://doi.org/10.1175/JPO2737.1.

Thomas, L. N., A. Tandon, and A. Mahadevan, 2008: Submesoscale Processes and Dynamics. *Geophysical Monograph Series*, **177**, 17–38, https://doi.org/10.1029/177GM04.

Thomas, L. N., and J. R. Taylor, 2010: Reduction of the usable wind-work on the general circulation by forced symmetric instability. *Geophysical Research Letters*, **37 (18)**, 18 606, https://doi.org/10.1029/2010GL044680.

Thomas, L. N., J. R. Taylor, E. A. D'Asaro, C. M. Lee, J. M. Klymak, and A. Shcherbina, 2016: Symmetric Instability, Inertial Oscillations, and Turbulence at the Gulf Stream Front. *Journal of Physical Oceanography*, **46 (1)**, 197–217, https://doi.org/10.1175/JPO-D-15-0008.1.

Thomas, L. N., J. R. Taylor, R. Ferrari, and T. M. Joyce, 2013: Symmetric instability in the Gulf Stream. *Deep Sea Research Part II: Topical Studies in Oceanography*, **91**, 96–110, https://doi.org/10.1016/J.DSR2.2013.02.025.

Wang, X., T. Kukulka, J. T. Farrar, A. J. Plueddemann, and S. F. Zippel, 2023: Langmuir Turbulence Controls on Observed Diurnal Warm Layer Depths. *Geophysical Research Letters*, **50 (10)**, e2023GL103 231, https://doi.org/10.1029/2023GL103231.

Wenegrat, J. O., 2023: The Current Feedback on Stress Modifies the Ekman Buoyancy Flux at Fronts. *Journal of Physical Oceanography*, **53 (12)**, 2737–2749, https://doi.org/10.1175/JPO-D-23-0005.1.

Wenegrat, J. O., J. Callies, and L. N. Thomas, 2018: Submesoscale Baroclinic Instability in the Bottom Boundary Layer. *Journal of Physical Oceanography*, **48 (11)**, 2571–2592, https://doi.org/10.1175/JPO-D-17-0264.1.

Wenegrat, J. O., and M. J. McPhaden, 2016: Wind, Waves, and Fronts: Frictional Effects in a Generalized Ekman Model. *Journal of Physical Oceanography*, **46 (2)**, 371–394, https://doi.org/10.1175/JPO-D-15-0162.1.

Wenegrat, J. O., and L. N. Thomas, 2020: Centrifugal and Symmetric Instability during Ekman Adjustment of the Bottom Boundary Layer. *Journal of Physical Oceanography*, **50 (6)**, 1793–1812, https://doi.org/10.1175/JPO-D-20-0027.1.

Wunsch, C., and R. Ferrari, 2004: Vertical mixing, energy, and the general circulation of the oceans. *Annual Review of Fluid Mechanics*, **36 (Volume 36, 2004)**, 281–314, https://doi.org/10.1146/ANNUREV.FLUID.36.050802.122121.

Yu, X., R. Barkan, and A. C. Naveira Garabato, 2024: Intensification of submesoscale frontogenesis and forward energy cascade driven by upper-ocean convergent flows. *Nature Communications*, **15 (1)**, 1–10, https://doi.org/10.1038/s41467-024-53551-4.

Yuan, J., and J. H. Liang, 2021: Wind- and Wave-Driven Ocean Surface Boundary Layer in a Frontal Zone: Roles of Submesoscale Eddies and Ekman–Stokes Transport. *Journal of Physical Oceanography*, **51 (8)**, 2655–2680, https://doi.org/10.1175/JPO-D-20-0270.1.

Zilitinkevich, S. S., 1972: On the determination of the height of the Ekman boundary layer. *Boundary-Layer Meteorology*, **3 (2)**, 141–145, https://doi.org/10.1007/BF02033914.

Zilitinkevich, S. S., I. Esau, N. Kleeorin, I. Rogachevskii, and R. D. Kouznetsov, 2010: On the velocity gradient in stably stratified sheared flows. Part 1: Asymptotic analysis and applications. *Boundary-Layer Meteorology*, **135 (3)**, 505–511, https://doi.org/10.1007/S10546-010-9488-X/METRICS.

Zippel, S. F., J. T. Farrar, C. J. Zappa, and A. J. Plueddemann, 2022: Parsing the Kinetic Energy Budget of the Ocean Surface Mixed Layer. *Geophysical Research Letters*, **49 (2)**, e2021GL095 920, https://doi.org/10.1029/2021GL095920.